2022-05-26

Design and prototyping of a low-cost light weight fixed-endpoint orientation planar Cobot

Howard, Ian

10.1109/icsse55923.2022.9947353
2022 International Conference on System Science and Engineering (ICSSE)
IEEE

Design and prototyping of a low-cost light weight fixed-endpoint orientation planar Cobot

Ian S. Howard
School of Engineering, Computing & Mathematics
University of Plymouth
Plymouth, UK
ian.howard@plymouth.ac.uk

Abstract—Here we present the design and construction of a low-cost planar robotic arm that makes use of light weight component and a passive link mechanism to maintain fixed endpoint orientation. The arm structure itself is low-cost and built from carbon fiber tubes which yields a high stiffness to weight ratio. To facilitate construction, commercially available pulley and bearing components are used in the design where possible and all custom mechanical parts are 3D printed. To reduce power consumption, the arm makes use of non-back-drivable worm-gear motor actuation, so static arm configurations can be maintained without requiring motor power. We first analyze and simulate the kinematics and the static torque/force relationships of the mechanism. A microcontroller system was then developed to read the sensors and drive the arm motors. Finally, we demonstrate arm operation with simple movement tasks.

Keywords—Worm-drive, 3D printing, Robot arm design, Agricultural robotics, Low-cost Cobot manipulator.

I. INTRODUCTION

A. Overview

Driven by shortages of agricultural workers and the continuous advances made in robotic technology, fruit and vegetable harvesting in now becoming a major application area for robotic technology [1]. Consequently, there is a strong business case for the deployment of a low-cost robotic berry picking solutions, to drive down the cost of harvesting and alleviate labor shortages Here we focus on the requirement of a robotic arm aimed for operation in the area of agricultural berry picking tasks. In this scenario, a robotic arm is generally mounted on a mobile platform that drives up and down structured locations (typically in a greenhouse), and identifies, picks and collects the ripe berries in an autonomous fashion as is passes by. There are many requirements for such a robot arm and generally they represent a compromise in design [2].

B. Requirements

Firstly, the robot arm should have a large enough workspace to reach the berries from its mobile platform. This necessitates the arm links are of sufficient length. However, since arm stiffness rapidly decreases with link length, a compromise needs to be made on the length of the arm links and the stiffness that is desirable, for a given arm cross-section and weight.

The arm should achieve sufficient accuracy and resolution in endpoint placement to reach a target berry location. High accuracy in the arm mechanism requires low play in the drive mechanism and also high stiffness in the arm structure. High accuracy would ensure this can be achieved without excessive online correction during movement, e.g. by using visual servoing [3]. In berry picking tasks, both accuracy and resolution will need to be of the order of millimeters, so the end-effector can be located to harvest a berry effectively.

The arm should be capable of generating sufficient endpoint force to pull a berry off a plant and move payloads, including end-effector picking mechanisms. A brute force approach to picking constitutes significant endpoint force requirement in the order of around 10 N (1Kgf) for a raspberry [4]. We note also that other removal techniques are also possible, including cutting [5].

The arm actuation and control should be power efficient since such mobile picking systems generally operate from batteries, although researchers are looking at ways to make use of solar power to recharge batteries when daylight conditions permit [6].

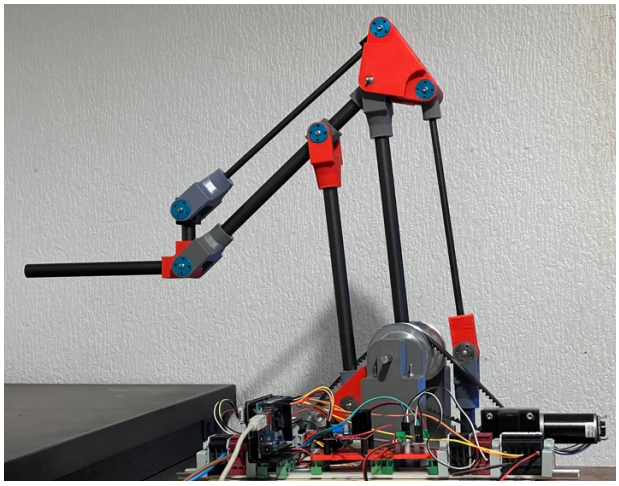

Figure 1. 2D planar revolute arm with passive 0° endpoint orientation mechanism. The main structure of the underlying 2DOF of freedom arm takes the form of a parallelogram. An additional parallelogram structure, located on the rear of the 2D arm structure, ensures the end effector maintains a constant orientation along the horizontal axis.

The arm should be safe to operate in the proximity of people and be able to deal with inevitable collisions that will occasionally occur with both people and other objects like the berry bush and its supports. In particular care has to be taken to ensure no one is injured and nothing is damaged by accidental collision. There are various ways of achieving this.

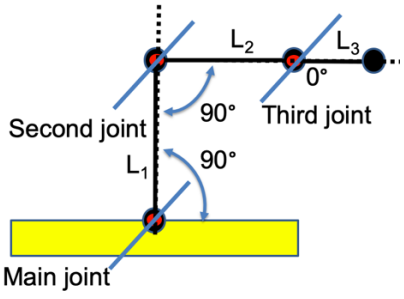

Figure 2. Default configuration of the 3-link arm showing joints.

Firstly, arms can be made inherently compliant [7,8]. This approach was taken with the Gummiarm [9,10]. However, the introduction of passive compliance can often affect performance. Reducing the moving mass and inertia of an arm makes it safer since less kinetic energy is stored in the arm as it moves, so it can do less damage on impact. A currently very popular approach is adopted in Cobots [11], which is to ensure force and torques generated by the robot do not exceed those expected for the task, and if they do so the robot detects the fault condition and appropriately shuts down.

Last but not least, the arm should be low-cost to ensure economic viability of an automated approach compared to human labor. This can be achieved by reducing the equipment deployment cost, which includes the cost of capital investment, as well as running and maintenance cost. This necessitates the use of a low-cost but well-engineered bespoke robotic arm solution, since many commercially available arms are too expensive to be viable. Competitiveness can also be enhanced by increasing the harvesting rate in berries per second. This can be achieved by using a faster and more accurate arm mechanism, and effective control strategies.

Figure 3. 2D arm. Enpoint alignment joint mechanism. A triangular mechanism is used to transfer motion of the passive arm to ensure the end effector always remains at a constant angular orientation.

II. PLANAR ARM MECHANISM

A. *Overview*

Here we build an arm that exhibits low mass and operate with a controller that can estimate motor torque at any point in time, thereby enabling us to build safety circuitry safety mechanism into the controller so that unexpected collisions can be detected. To keep the weight of the mechanism down, the upper and lower arm section were constructed from 16x14mm diameter carbon fiber tubing (length 250mm).

To reduce mechanism complexity and simplify control, we design a two-dimensional mechanism that can maintain and orientation a constant endpoint orientation. Autodesk Fusion 360 was used to design all custon parts.

B. *2DOF Parallelogram design*

As shown in Figs. 1 and 2, the arm consists of a parallelogram structure which is driven from the main joint axis via two timing belts. In practice the arm mechanism would be also mounted on a 3rd degree of freedom, to generate a 3D workspace. Details of the arm joint mechanisms used are shown in Figs. 3 – 5. The stiff and low mass parallelogram architecture of the current arm is similar to that adopted in the VBot robotic manipulandum, which is a research tool used for investigating human movement [12].

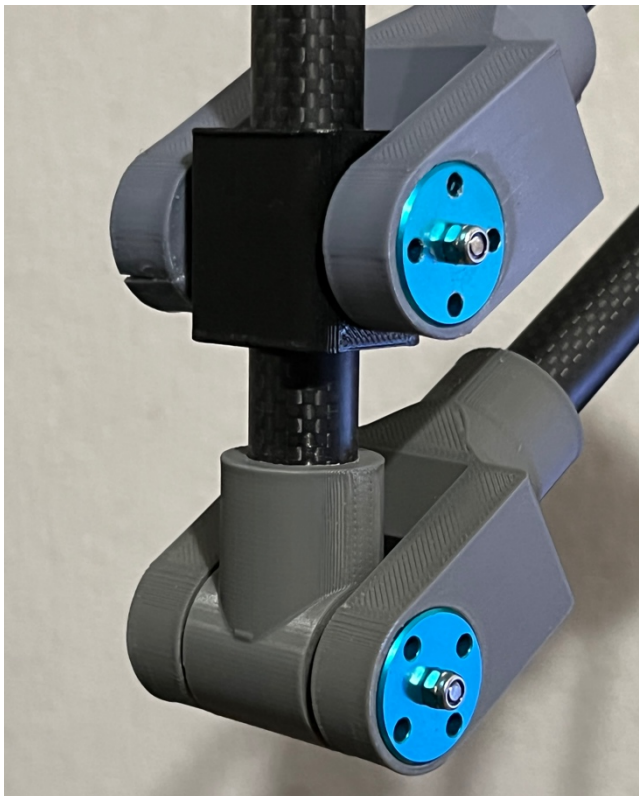

Figure 4. 2D arm joints. The arm joints constitute a critical part of the design of the arm mechanism, since the use of small ballbearings ensures very low joint friction and the use of aluminum flanges and 3D printed parts realized a precise mechanism which exhibits low mass.

The main lower arm is driven directly from its corresponding timing pulley. Similarly, the short secondary arm, custom made from PLA, is also driven by a timing pulley The upper arm forms the upper part of the parallelogram. The upper arm is connected to the lower via two fork joints, one of which is shown in Fig. 5. The carbon fiber tubes were attached to the PLA joint components using Loctite superglue.

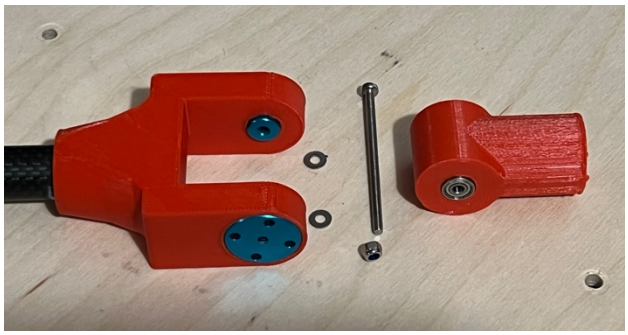

Figure 5. Arm joint components. The upper link of the arm Section shown in the RHS of the Figure contains 3 mm internal diameter ball bearing races. This joint assembly is held within a fork on the LHS which makes use of aluminum flanges. These are used to support the shaft and interface to the bearings because of their superior mechanical properties over plastic. An M3 bolt is used to locate the bearing assembly to the fork and to firmly secured it using a nylon locknut. Stainless steel washers are used between the flanges and the bearings to achieve suitable joint clearance.

In order to ensure the third arm link and therefore the endpoint maintains a constant orientation, another passive link mechanism is located at the back of both the lower and upper arms. In this way the mechanism is able to control position and maintain orientation of the end effector by controlling only 2 degrees of freedom.

C. *Worm-drive motor actuation*

To reduce power consumption, we make use of mass-produced low-cost worm-gear motor actuation. They are well suited to the current application because they deliver high-torque and their non-back drivable nature of such drives ensures that static joint configuration can be maintained without requiring motor power [13]. The latter makes the design power-efficient and well suited to mobile operation running from batteries.

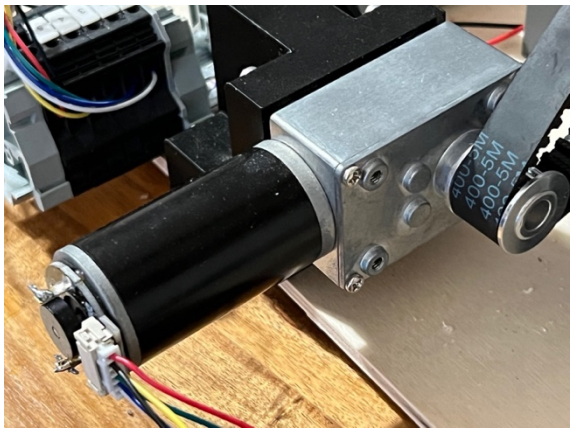

Figure 6. Worm-drive DC motor. The worm drive motor realizes a substantial mechanical advantage in a small space and also constitutes an actuation system that is not back-drivable. The latter ensures the arm can maintain a static posture without power requirement.

Worm gear motors rotate timing pulleys (see Fig. 6) located and drive the main joint axis via timing belts. The worm drive motors are mounted on a baseplate. This ensures considerable torque is delivered to the main axes of the arm without backlash, leading in high force at the end effector.

The worm drive motors incorporate Hall effect encoders at the rear of the DC motors prior to gear reduction so the rotational angle of the DC worm drive motors can be sensed. Consequently, the output shaft of the worm drive motors can be resolved to a high angular resolution of about 4000 pulses per revolution. The worm drive motors themselves operate at 24V and typically draw up to 1A under full load. They have a gearing ratio of 280 leading to no-load rotational output shaft speed of 28RPM and at a rated output torque of 5Nm. The output shafts of the motors are connected to the drive axes of the planar arm using T5 10mm wide timing belts, with 12 and 40 teeth pulleys on the motor shaft and robot axes respectively. This gives an additional reduction in rotational speed of 3.33 and also a corresponding increase in torque.

For the selected motor, the maximum speed of the of each driven joint is given by maximum motor rotational speed in RPM divided by the mechanical advantage of the pulleys, then converted to radians per second

$$\omega_{max} = 28 * \left(\frac{12}{40}\right) * \left(\frac{2\pi}{60}\right) = 0.88\ Rads^{-1} \qquad (1)$$

Similarly, the maximum torque of the of each driven joint is given by maximum motor rotational torque in Nm scaled by the mechanical advantage of the pulleys

$$\tau_{max} = 5 * \left(\frac{40}{12}\right) = 16.7\text{Nm} \qquad (2)$$

III. KINEMATIC ANALYSIS

The analysis of forward and inverse kinematics of revolute planar arm mechanisms are available in many textbooks on robotics [14 -17]. We also include simple derivations here for the convenience of the reader.

A. *Denavit-Hartenberg analysis*

The kinematic structure of the 3-links of the arm is shown in Fig. 7. Although the kinematics can be derived easily from the arm geometry, here we adopt a formal approach. Suitable frames for Denavit-Hartenberg (DH) analysis are shown in Fig.8. This leads to the classical DH table shown in Table 1. In particular, we note that as the arm is planar, the link twist angle α is always zero and the offset d between links is also always zero. The link lengths for the current design are L1 = 300mm; L3 = 300mm and L3 = 100mm.

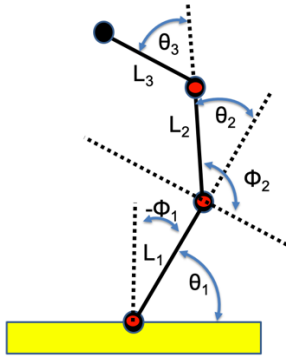

Figure 7. General configuration defined in terms of link lengths L_1, L_2 L_3 and corresponding joint angles θ_1, θ_2, θ_3. The joint angles Φ_1, Φ_2 are defined with respect to the default configuration.

TABLE 1. DENAVIT-HARTENBERG TABLE, INCLUDING JOINT RANGE LIMITS, FOR THE 3-LINK PLANAR ARM WRITTEN IN TERMS OF LINK LENGTH AND DIRECT Z-AXIS ROTATION ANGLES

Link	Angle θ [°]	Min θ [°]	Max θ [°]	Angle α [°]	Radius a [mm]	Offset d [mm]
1	θ_1	35°	145°	0	300	0
2	θ_2	-145°	-35°	0	300	0
3	θ_3			0	100	0

A classical DH-frame i can be represented by the homogenous transformation matrix, written here in shorthand, where c refers to cosine and s to sine.

$$A_i = \begin{bmatrix} c\theta_i & -s\theta_i c\propto_i & s\theta_i s\propto_i & a_i c\theta_i \\ s\theta_i & c\theta_i c\propto_i & -c\theta_i s\propto_i & a_i s\theta_i \\ 0 & s\propto_i & c\propto_i & d_i \\ 0 & 0 & 0 & 1 \end{bmatrix} \qquad (3)$$

We note that in our case since $\propto = 0$ the terms $c\propto = 1$ and $S\propto = 0$. Therefore, the homogeneous transformation for a single link simplifies to the expression:

$$A_i = \begin{bmatrix} c\theta_i & -s\theta_i & 0 & a_i c\theta_i \\ s\theta_i & c\theta_i & 0 & a_i s\theta_i \\ 0 & 0 & 1 & 0 \\ 0 & 0 & 0 & 1 \end{bmatrix} \quad (4)$$

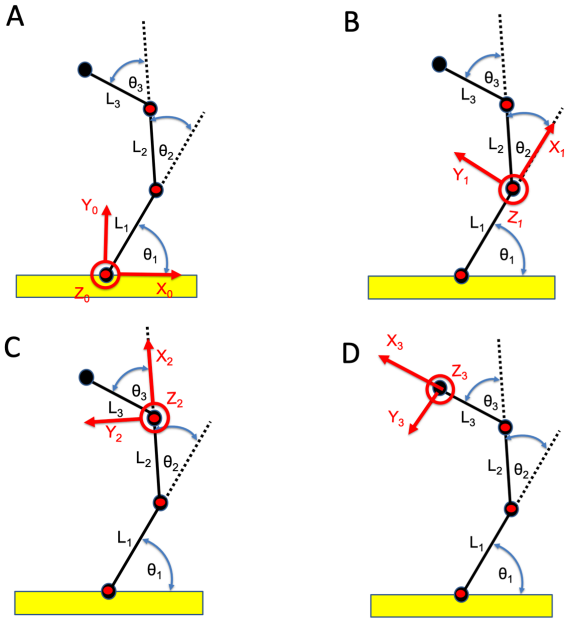

Figure 8. Denavit-Hartenberg co-ordinate frames for 3-link planar arm defined in terms of link lengths L_1, L_2 L_3 and corresponding joint angles θ_1, θ_2, θ_3.

B. *Forward kinematics*

Mapping from frames 3 to base frame 0 is achieved using the product of homogeneous matrices for the three links

$$^0_3H = {}^0_1H\,{}^1_2H\,{}^2_3H \quad (5)$$

Here we make use of MATLAB symbolic toolbox to simplify the matrix equations. This leads to the overall homogeneous transformation

$$^0_3H = \begin{bmatrix} c_{123} & -s_{123} & 0 & L_1c_1 + L_2c_{12} + L_3c_{123} \\ s_{123} & c_{123} & 0 & L_1s_1 + L_2s_{12} + L_3s_{123} \\ 0 & 0 & 1 & 0 \\ 0 & 0 & 0 & 1 \end{bmatrix} \quad (6)$$

Where L_1, L_2 and L_3 represent the three link lengths, and we use the further following simplifying notation:$c_1 = \cos(\theta_1)$, $s_1 = \sin(\theta_1), c_{12} = \cos(\theta_1 + \theta_2), s_{12} = \sin(\theta_1 + \theta_2), c_{123} = \cos(\theta_1 + \theta_2 + \theta_3), s_{123} = \sin(\theta_1 + \theta_2 + \theta_3)$.

The endpoint position of the 3rd link is therefore given by the expression

$$\begin{bmatrix} x \\ y \end{bmatrix} = \begin{bmatrix} L_1c_1 + L_2c_{12} + L_3c_{123} \\ L_1s_1 + L_2s_{12} + L_3s_{123} \end{bmatrix} \quad (7)$$

In our implementation, the angle θ_3 is not a free parameter and is determined by the desired link orientation angle θ_{end} and the angles θ_1 and θ_2. More precisely

$$\Rightarrow \theta_{\text{end}} = \theta_1 + \theta_2 + \theta_3 \quad (8)$$

The endpoint position of the 3rd link is therefore given by the expression

$$\begin{bmatrix} x \\ y \end{bmatrix} = \begin{bmatrix} L_1c_1 + L_2c_{12} + L_3c_{\text{end}} \\ L_1s_1 + L_2s_{12} + L_3s_{\text{end}} \end{bmatrix} \quad (9)$$

where θ_{end} is the require constant orientation angle of the 3rd link, $s_{\text{end}} = \sin(\theta_{\text{end}})$ and $c_{\text{end}} = \cos(\theta_{\text{end}})$. In our arm mechanism the orientation of the end link is set at a constant orientation along the x-axis, so $\theta_{\text{end}} = 0$. This this leads to a simplification in the homogeneous transformation mapping from frames 3 to base frame 0:

$$^0_3H = \begin{bmatrix} 1 & 0 & 0 & L_1c_1 + L_2c_{12} + L_3 \\ 0 & 1 & 0 & L_1s_1 + L_2s_{12} \\ 0 & 0 & 1 & 0 \\ 0 & 0 & 0 & 1 \end{bmatrix} \quad (10)$$

We note that the rotation matrix component is the identity matrix, since the endpoint orientation of the arm remains constant as arm configuration is changed. Also, there is a translational offset in the x-axis arising from the length of the third link, as can be verified by observation of the arm geometry.

The default configuration of the arm is shown in Fig. 2, and its general configuration in Fig 7. The default configuration can be used to define operating angles that deviate from it, as shown. In the default configuration, the control angles Φ_1 and Φ_2 are both zero. It can be seen there is a simple relationship between the joint angles θ_1, θ_2, and the control angles Φ_1, Φ_2. Namely that

$$\theta_1 = \Phi_1 + 90° \quad (11)$$

$$\theta_2 = \Phi_2 - 90° \quad (12)$$

We note that the DH table can easily be re-written by substituting in these control angles, as shown in table 2.

TABLE 2. DENAVIT-HARTENBERG TABLE FOR THE 3-LINK PLANAR ARM WRITTEN IN TERMS OF LINK LENGTH CONTROL AXIS ROTATION ANGLES

Link	Angle θ [°]	Min Φ [°]	Max Φ [°]	Angle α [°]	Radius a [mm]	Offset d [mm]
1	90° + Φ_1	-55°	55°	0	300	0
2	Φ_2 - 90°	-55°	55°	0	300	0
3	θ_{end} - θ_2 - θ_1			0	100	0

C. *Workspace*

The main robot arm axis can in principle rotate from approximately 0° to 180°. However due to constraints in the endpoint orientation mechanism, it is limited to 35° to 145°. The secondary joint is also limited by its parallelogram mechanism and can rotate by approximately between -35° to -145°. This workspace of the end of the 2-link structure shown in red on Fig. 9. This is contrasted with the workspace when the passive arm limitations are considered, as shown in green.

The effect of the third linkage, which is maintained at a constant orientation angle, is to extend the workspace with a linear translation, as illustrated in Fig. 10 for an end orientation of 0°. This causes a translation along the horizontal x-axis. With an end orientation of 90° this translation would occur along the y-axis although it could easily be made to occur in both x and y, simply by changing the orientation angle chosen for the third link.

D. *Inverse kinematics*

Inverse kinematics for a 2-link arm mechanism can be derived analytically using the cosine rule. Here, we wish to find arm angles (θ_1, θ_2) given endpoint locations (x_2, y_2). Pythagoras theorem gives

$$r^2 = x_2^2 + y_2^2 \quad (13)$$

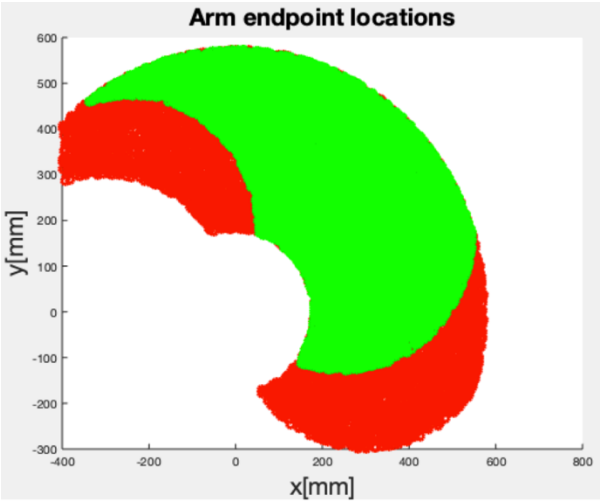

Figure 9. Workspace of the endpoint of the main 2-link mechanism of arm, given links lengths of 300mm. The red area shows the range of the arm section without limitation of the passive orentation mechanism. It exhibits angular ranges of 0° to 180° for the main axis and -35° to -145° for the secondary axis respectively. Green plot shows the range of the 2D arm section including the limitation imposed by the passive arm mechanism, which reduces the main axis movement range to angular range between 35° to 145°.

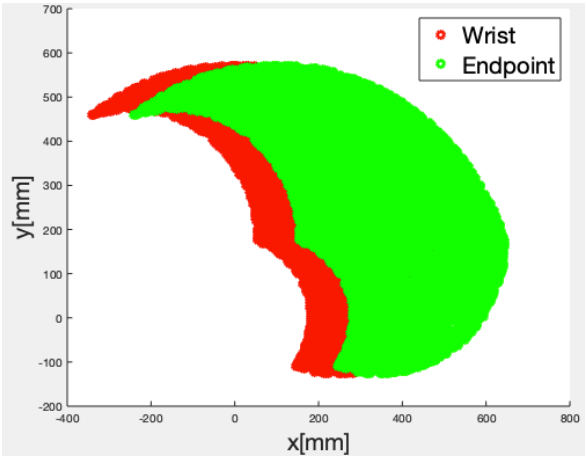

Figure 10. Workspace shift (from red to green areas) of the endpoint of the 2-link mechanism of arm resulting from using the 3rd link which is maintained at a constant angular orientation $\theta_{end} = 0°$ by the passive orientation mechanism.

From Fig. 11A, and using the cosine rule equation we can write an expression for cos(α) in terms of known quantities (x_2, y_2) and L_1, L_2.

$$r^2 = L_1^2 + L_2^2 - 2L_1L_2\cos(\alpha) \quad (14)$$

$$\Rightarrow \cos(\alpha) = \frac{L_1^2 + L_2^2 - x_2^2 - y_2^2}{2L_1 L2} \quad (15)$$

To derive the expression for cos(θ_2) from Fig 11A we note that

$$\theta_2 = \pi - \alpha \quad (16)$$

We also note that

$$\cos(\pi - \alpha) = -\cos(\alpha) \quad (17)$$

$$\Rightarrow \cos(\theta_2) = \frac{x_2^2 + y_2^2 - L_1^2 - L_2^2}{2L_1 L_2} \quad (18)$$

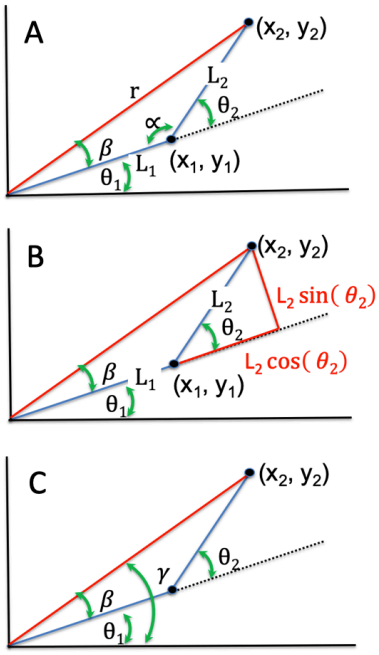

Figure 11. Schematics of 2D revolute planar arm useful for the derivation of inverse kinematics, showing relevant positions, angles and lengths.

From Fig. 11B from the right-hand triangle that has angle β we see that

$$\tan(\beta) = \frac{L_2\sin(\theta_2)}{L_2\cos(\theta_2) + L_1} \quad (19)$$

$$\Rightarrow \beta = \operatorname{atan}\left[\frac{L_2\sin(\theta_2)}{L_2\cos(\theta_2) + L_1}\right] \quad (20)$$

We make use of angle β derive the expression for angle θ_1. Also, as indicated by geometric considerations as shown on Fig. 11C

$$\theta_1 = \gamma - \beta \quad (21)$$

$$\gamma = \operatorname{atan}\left[\frac{y_2}{x_2}\right] \quad (22)$$

$$\Rightarrow \theta_1 = \operatorname{atan}\left[\frac{y_2}{x_2}\right] - \operatorname{atan}\left[\frac{L_2\sin(\theta_2)}{L_2\cos(\theta_2) + L_1}\right] \quad (23)$$

To arrive at the final equations for the inverse kinematics from the overall endpoint (x_3, y_3) to the joint angles (θ_1, θ_2) we need to account for the constant orientation link in the 3-link design. To do so we simply need to subtract the link length L_3 from the x_3 position value and use the y values as it is:

$$\begin{bmatrix} x_2 \\ y_2 \end{bmatrix} = \begin{bmatrix} x_3 - L_3 \\ y_3 \end{bmatrix} \quad (24)$$

We now substitute the values into eqns. (18, 23)

$$\Rightarrow \theta_1 = \operatorname{atan}\left[\frac{y_3}{(x_3 - L_3)}\right] - \operatorname{atan}\left[\frac{L_2\sin(\theta_2)}{L_2\cos(\theta_2) + L_1}\right] \quad (25)$$

$$\Rightarrow \theta_2 = \pm\operatorname{acos}\left[\frac{(x_3 - L_3)^2 + y_3^2 - L_1^2 - L_2^2}{2L_1 L_2}\right] \quad (26)$$

We notice that eqn. (26) has two solutions and that the value of θ_2 is used to calculate θ_1 using eqn. (25). Here we use the negative solution for θ_2 since it corresponds to the operating configuration of our arm design (as shown in Fig 2).

IV. VELOCITY AND FORCE RELATIONSHIPS

To calculate the velocity and torque/force relationships between the control joints and endpoint, we first derive the 2x3 Jacobian matrix of the endpoint position with respect to the angles θ_1, θ_2 and θ_3 which has the form:

$$J = \begin{bmatrix} \frac{\partial x}{\partial \theta_1} & \frac{\partial x}{\partial \theta_2} & \frac{\partial x}{\partial \theta_3} \\ \frac{\partial y}{\partial \theta_1} & \frac{\partial y}{\partial \theta_2} & \frac{\partial y}{\partial \theta_3} \end{bmatrix} \tag{27}$$

We derive the Jacobian on the basis of general expression for end position in eqn. (7) in which all three angles are variables.

$$\frac{\partial x}{\partial \theta_1} = -L_1 s_1 - L_2 s_{12} - L_3 s_{123} \tag{28}$$

$$\frac{\partial x}{\partial \theta_2} = -L_2 s_{12} - L_3 s_{123} \tag{29}$$

$$\frac{\partial x}{\partial \theta_3} = -L_3 s_{123} \tag{30}$$

$$\frac{\partial y}{\partial \theta_1} = L_1 c_1 + L_2 c_{12} + L_3 c_{123} \tag{31}$$

$$\frac{\partial y}{\partial \theta_2} = L_2 c_{12} + L_3 c_{123} \tag{32}$$

$$\frac{\partial y}{\partial \theta_3} = L_3 c_{123} \tag{33}$$

We can differentiate the expression for overall endpoint orientation θ_{end} given by eqn. (8) and using eqns. (28-33) and thereby write a 3x3 Jacobian and use it compute the endpoint linear and rotational velocities from the joint velocities:

$$J = \begin{bmatrix} -L_1 s_1 - L_2 s_{12} - L_3 s_{123} & -L_2 s_{12} - L_3 s_{123} & -L_3 s_{123} \\ L_1 c_1 + L_2 c_{12} + L_3 c_{123} & L_2 c_{12} + L_3 c_{123} & c_{123} \\ 1 & 1 & 1 \end{bmatrix} \tag{34}$$

$$\begin{bmatrix} \dot{x} \\ \dot{y} \\ \dot{\theta}_{end} \end{bmatrix} = J \begin{bmatrix} \dot{\theta}_1 \\ \dot{\theta}_2 \\ \dot{\theta}_3 \end{bmatrix} \tag{35}$$

Insight can be derived from the Jacobian of the arm mechanism. The determinant of the Jacobian is given by

$$\det(J) = \mathrm{L}_1 \mathrm{L}_2 s_2 \tag{36}$$

We notice that the determinant is zero when $\theta_2 = \{0, \pi\}$ which occur when the second link either aligns with or folds back on the first link. These values are outside the operational range of the arm. Therefore, we can use the inverse Jacobian to invert eqn. (35) and calculate the joint angular velocities:

$$\begin{bmatrix} \dot{\theta}_1 \\ \dot{\theta}_2 \\ \dot{\theta}_3 \end{bmatrix} = J^{-1} \begin{bmatrix} \dot{x} \\ \dot{y} \\ \dot{\theta}_{end} \end{bmatrix} \tag{37}$$

We also note that the 2x3 Jacobian in eqn. (27) can be used to relate joint torques, written as $[\tau_1 \quad \tau_2 \quad \tau_3]^T$, to endpoint forces $[f_x \quad f_y]^T$ using the relationships:

$$\begin{bmatrix} \tau_1 \\ \tau_2 \\ \tau_3 \end{bmatrix} = J^T \begin{bmatrix} f_x \\ f_y \end{bmatrix} \tag{38}$$

V. CONTROL ELECTRONICS

A. Motor controller

A controller was built to actuate the arm and drive the worm drive motors based on the Arduino Mega. This has sufficient digital I/O with interrupts so that two incremental encoders on the rear of the motors can interface with it by means of interrupt pins. In this way it was easy to determine the position of the motors prior to gearing reduction by the worm drives. Using a L298N H-bridge ensured it is possible to reverse the direction of the rotation of the motors. The control drive to the H-bridge was operated using pulse-width-modulation (PWM) in order to set output rotational speed of the DC motors in an efficient fashion. To estimate the torque of the motors, drive current was measured using Hall sensors and was read-in via analog microcontroller inputs. To give an estimate of the mean current, a simple RC smoothing networks were employed. A schematic of the controller is shown in Fig. 12. The connections are given in Fig 13 and a photograph of its hardware realization in shown in Fig. 14. After calibration the micro controller was able to estimate motor shaft angular position of the motors, current flowing through the motors to estimate their torque output, and set input voltage to the DC motors. This forms the basis for effective control of the robotic arm.

VI. RESULTS

A. Simulation

To demonstrate the operation of inverse kinematics we generated a trajectory consisting of 100 points equally spaced around the circumference of a circle centered at (x,y) coordinates (0.42, 0.2) m and of radius 0.18m, that just fits into the workspace of the arm. We used the inverse model to calculate the appropriate arm angles to reach points on the circle. Fig 15 shows target circle and the arm configuration to reach 3 selected points.

Using eqn. (37), we calculate the angular velocities at the motor shafts for 1 rotation of the endpoint around the circle per second. Fig 16 shows the corresponding velocity plots. It can be seen the maximum joint speed of 0.60 Rad/s is less than that the maximum the motors can achieve, as indicated by eqn. (2). We note that following the target circle using the end of the 2-link arm by means of inverse kinematics and using finite differences to calculate velocities, yields the same results.

Using eqn. (38), and ignoring the contribution from the intrinsic the arm dynamics, which is of course is only valid at low movement speeds, we calculate the torques at the motor shafts needed to support a realistic 1kg payload and pull with 1Kgf in the horizontal directions simultaneously, for endpoint locations around the target circle. The vertical force represents the effect of gravity on a 1kg payload. From Fig. 17, it can be seen the maximum joint torque value of around 8.56Nm is less than the rated joint torque that can be delivered by the motors (16.7Nm), as indicated in eqn. (2).

B. *Operating physical robotic arm*

Simple movement tests were carried out on the physical robot using PD control of the motor angles computed using inverse kinematics of the endpoint target position trajectories using eqns. (25,26). Operation of the robotic arm is shown on the YouTube channel: Robotics, Control and Machine Learning in the playlist: ICSSE2022 & NSSSE2022 2D CF Robot Arm

https://youtube.com/playlist?list=PLjKvJX8cBCKW8gDLd7jTcET0vT0sUzQMS

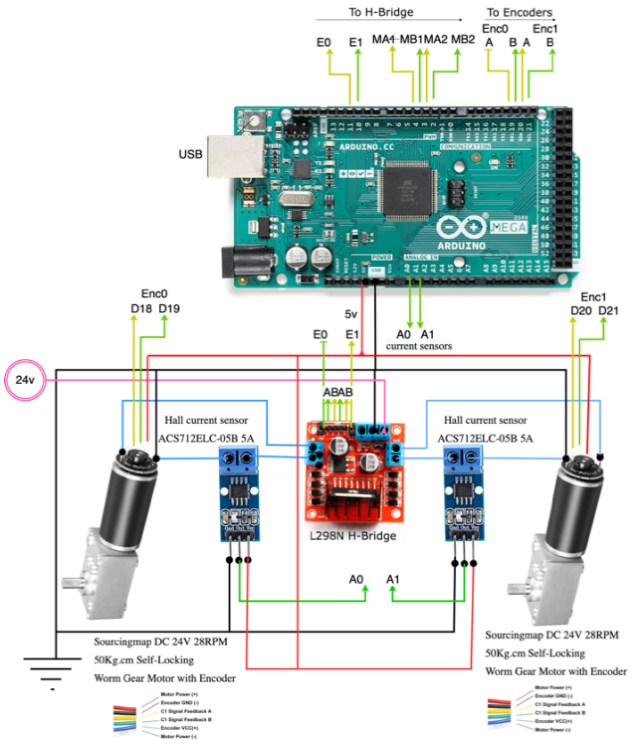

Figure 12. Schematic of Arduino Mega based controller connections. The Mega micro-controller generate output PWM and direction signals for the dual H-bridge which drive the two worm drive DC motors. In addition it reads the encoder is on the back of each of the worm drive motors, and it reads the current passing through each of the DC motors measured by the Hall current sensors. The H-bridge current for the motors runs from a 24v power line. The 5v supply also needed to drive H-bridge and Hall current sensors is supplied by the Arduino Mega.

Arduino Mega Pin	Description		Pin		Component
D2	Digital output		CH1 A	H Input	L288 H-Bridge
D3	Digital output		CH1 B	H Input	
D9	Digital output PWM		CH1Enable	Enable	
D4	Digital output		CH2 A	H Input	
D5	Digital output		CH2 B	H Input	
D10	Digital output PWM		CH2Enable	Enable	
A0	Analog input		out	Current measurement	Hall current sensor CH2
A1	Analog input		out	Current measurement	Hall current sensor CH2
D18	Digital input IR		A signal	Pulse	Encoder CH1
D19	Digital input IR		B signal	Pulse	
D20	Digital input IR		A signal	Pulse	Encoder CH2
D21	Digital input IR		B signal	Pulse	

Figure 13. Arduino Mega pin connections

VII. DISCUSSION

A. *Summary*

Here we developed a lightweight two-dimensional workspace robotic mechanism with use in the agriculture industry in mind, but which could be also applied in other industries. Worm-drive actuation was adopted since it ensures static posture can be maintained without requiring active motor drive, thereby reducing power consumption. The use of off-the-shelf components makes the design cost-effective and its inherent low moving mass makes it relatively safe to operate around people. The safety aspect is further enhanced by monitoring control current, which can then be compared to expected values for a given task and deactivate the control if the values are exceeded.

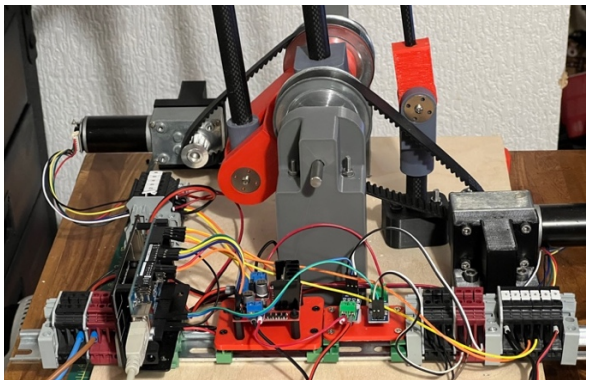

Figure 14. Control of the robot is realized using an Arduino Mega micro controller mounted on a DIN rail. The microcontroller is interfaced to the arm's motors and sensors. A L298N Dual H-bridge is employed to operate DC motors. The current drawn by the DC motors is measured using ACS712 5ADC Hall effect current sensors which are interfaced back with the Arduino Mega via analog inputs. Incremental encoders are directly connected to the Arduino Mega in order to measure the position of the DC motor shafts.

B. *Future improvements*

In the future the current mechanism will also be mounted on a third rotary axis in order to achieve full 3D space coverage.

We note using direct drive brushless DC motors instead of worm-drive DC motors would have the potential to considerably improve torque estimation, and system performance in general, but at the expense of higher cost and static configuration power drain.

We made use of 3D printed parts fabricated in PLA. Although this is a common material choice for prototyping, for actual deployment e.g., for picking fruit, more robust and environmentally resistant materials could easily be substituted, such as PETG, ABS or nylon. The stiffness of arm mechanism could easily be increased by making use of readily available carbon fiber tubes with a thicker wall section.

Currently angular position of the worm drive motor shafts is measured using incremental encoders. This enables the relationship of endpoint position to the motor angles using forward and inverse kinematics. However, this does not account for any bending and give in the arm mechanism itself. Adding additional light magnetic encoders on the arm axes would enable endpoint position to the estimated with greater accuracy.

There are many other ways of implementing safety features in robotic arms other than force monitoring adopted in Cobots [11]. Some approaches, in particular the Gummi-arm, have used co-contracting tendons which offer a means to implement passive variable stiffness actuation [9,10] and some recent work has investigated the dynamics and control

of such a joint using state feedback control [18] and industrial controllers [19]. Passive compliance has a big advantage of making a mechanism resistant to impulsive disturbances, such as physical knocks, which are hard to deal with active compliance due to the limited controller bandwidth. In the future we shall also look into incorporating some level of series elasticity [20] into the actuator design to increase its robustness.

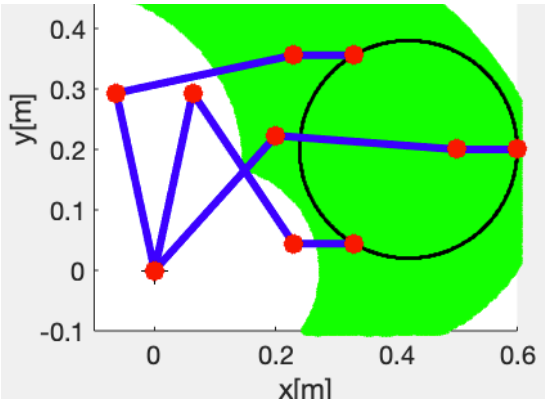

Figure 15. Visualization of the 3-link arm configurations used to reach 3 points on a target circle, with arm joint angles calculated using inverse kinematics. Part of the workspace of the arm is shown in green.

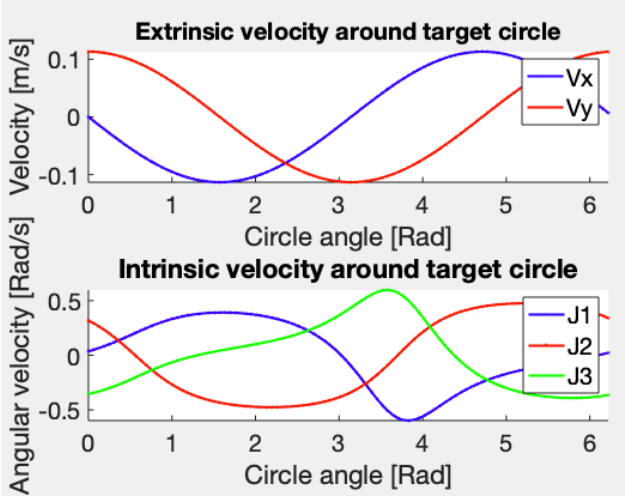

Figure 16. Arm velocity relationships during simulated movement of arm endpoint around target circle once in 10s. A) Arm extrinsic enpoint velocities B) Arm joint angular velocities.

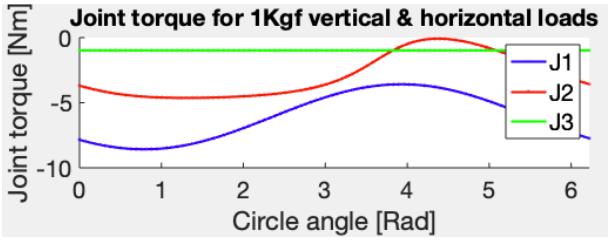

Figure 17. Simulated torques at the three joints shafts for 1Kgf static load in the horizontal direction whilst supporting a 1Kg payload, as endpoint moves around the target circle.

ACKNOWLEDGMENTS

We thank Enterprise Solutions at the University of Plymouth for financially supporting this work with a project entitled "Low-cost compliant robotic arm for fruit and vegetable harvesting". We also thank our industrial partner Fieldwork Robotics Ltd., and in particular Martin Stoelen (who is also at the Western Norway University of Applied Science), for their support and helpful discussion. Thanks also to Hooman Samani for commenting on the manuscript.

REFERENCES

[1] T. Duckett S. Pearson, S. Blackmore, B. Grieve W.H. Chen, G. Cielniak .. & G.Z. Yang, (2018). Agricultural robotics: the future of robotic agriculture. arXiv preprint arXiv:1806.06762.

[2] A. Bechar & C. Vigneault (2016). Agricultural robots for field operations: Concepts and components. Biosystems Engineering, 149, 94-111.

[3] F. Chaumette, S. Hutchinson, & P. Corke (2016). Visual servoing. In Springer Handbook of Robotics (pp. 841-866). Springer, Cham

[4] D.F. Kutz, Wölfel, A., Meindl, T., Timmann, D., & Kolb, F.P. (2009). Spatio-temporal human grip force analysis via sensor arrays. Sensors, 9(8), 6330-6345.

[5] B. Jia, A. Zhu, S.X. Yang & G.S. Mittal,(2009). Integrated gripper and cutter in a mobile robotic system for harvesting greenhouse products. In 2009 IEEE International Conference on Robotics and Biomimetics (ROBIO) (pp. 1778-1783). IEEE.

[6] S. Gorjian, H. Ebadi, M. Trommsdorff, H. Sharon, M. Demant & S. Schindele (2021). The advent of modern solar-powered electric agricultural machinery: A solution for sustainable farm operations. Journal of Cleaner Production, 292, 126030.

[7] B. Vanderborght, A. Albu-Schäffer, A. Bicchi, E. Burdet, D.G. Caldwell, R. Carloni, M.G. Catalano, O. Eiberger, W. Friedl, G. Ganesh. & M. Garabini, (2013). Variable impedance actuators: A review. Robotics and autonomous systems, 61(12), pp.1601-1614. and Control (ICAC3) (pp. 1-5). IEEE.

[8] G. Grioli, S. Wolf, M. Garabini, M. Catalano, E. Burdet, D. Caldwell, & A. Bicchi. (2015). Variable stiffness actuators: The user's point of view. The International Journal of Robotics Research, 34(6), 727-743.

[9] M.F. Stoelen, F. Bonsignorio. and A. Cangelosi, (2016), August. Co-exploring actuator antagonism and bio-inspired control in a printable robot arm. In International Conference on Simulation of Adaptive Behavior (pp. 244-255). Springer, Cham.

[10] M.F. Stoelen, R. de Azambuja, B. Lopez Rodriguez, F. Bonsignorio, & A. Cangelosi. (2022), The GummiArm Project: A Replicable and Variable-Stiffness Robot Arm for Experiments on Embodied AI. *Frontiers in Neurorobotics*, 24.

[11] J.E. Colgate, J. Edward, M.A. Peshkin, & W. Wannasuphoprasit (1996). Cobots: Robots for collaboration with human operators.

[12] I.S. Howard, J.N. Ingram & D.M. Wolpert (2009). A modular planar robotic manipulandum with end-point torque control. *Journal of neuroscience methods*, *181*(2), 199-211.

[13] V.H. Pinto, J. Gonçalves & P. Costa (2020).Model of a DC motor with worm gearbox. In Portuguese Conference on Automatic Control (pp. 638-647). Springer, Cham.

[14] B. Siciliano, L. Sciavicco, L. Villani & G. Oriolo, (2009). Robotics: Modelling, Planning and Control, 523-559.

[15] K. M. Lynch & F. C. Park, (2017). Modern robotics. Cambridge University Press.

[16] M. W. Spong, S. Hutchinson, & M. Vidyasagar, (2006). Robot modeling and control (Vol. 3, pp. 75-118). New York: Wiley.

[17] P.I. Corke & O. Khatib, O. (2011). Robotics, vision and control: fundamental algorithms in MATLAB (Vol. 73, p. 2). Berlin: Springer

[18] I.S. Howard & M. F. Stoelen, State space analysis of variable-stiffness tendon drive with non-back-drivable worm-gear motor actuation, TAROS 2021, (2021).

[19] I.S. Howard & M. F. Stoelen, EtherCAT implementation of a variable-stiffness tendon drive with non-back-drivable worm-gear motor actuation, TAROS 2021, (2021).

[20] G.A. Pratt & M.M. Williamson, (1995). Series elastic actuators. In Proceedings 1995 IEEE/RSJ International Conference on Intelligent Robots and Systems. Human Robot Interaction and Cooperative Robots (Vol. 1, pp. 399-406). IEE.